

## SUPPLEMENTARY INFORMATION

### Quantum error correction of spin quantum memories in diamond under a zero magnetic field

Takaya Nakazato,<sup>1</sup> Raustin Reyes,<sup>1</sup> Nobuaki Imaike,<sup>1</sup> Kazuyasu Matsuda,<sup>1</sup> Kazuya Tsurumoto,<sup>1</sup>

Yuhei Sekiguchi,<sup>2</sup> and Hideo Kosaka<sup>1,2\*</sup>

<sup>1</sup>Department of Physics, Graduate School of Engineering Science, Yokohama National University,  
79-5 Tokiwadai, Hodogaya, Yokohama 240-8501, Japan

<sup>2</sup>Institute of Advanced Sciences, Yokohama National University, 79-5 Tokiwadai, Hodogaya,  
Yokohama 240-8501, Japan

\*kosaka-hideo-yp@ynu.ac.jp

**Supplementary Note 1: Carbon spin manipulation.** We describe in detail the method of the simulation in Fig. 1c of the main text. First, we assume a situation where a magnetic field is applied along the NV axis. With the direction of the external magnetic field as the quantization axis of carbon nuclear spins, the Hamiltonian of the electron spin and two carbon nuclear spins can be described as follows,

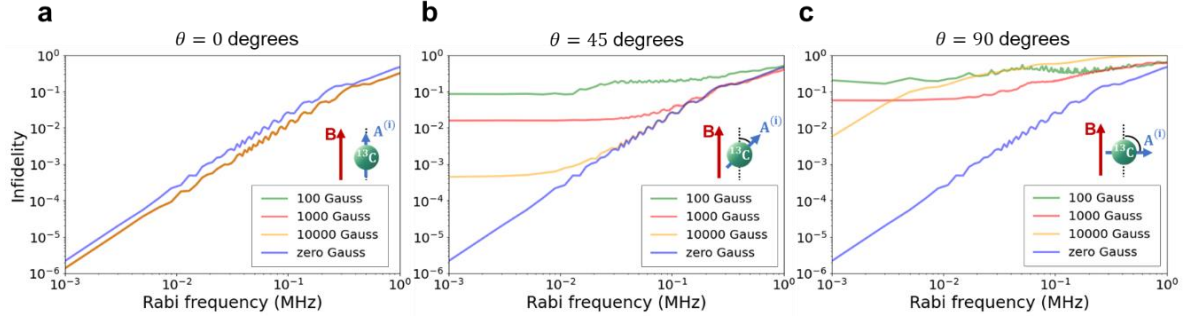
$$H = D_0 S_z^2 + \gamma_e B_z S_z + \sum_{i=1}^2 \left( \gamma_c B_z I_z^{(i)} + A_{\parallel}^{(i)} S_z I_z^{(i)} + A_{\perp}^{(i)} S_z I_x^{(i)} \right), \quad (1)$$

where  $\mathbf{S} = (S_x, S_y, S_z)$  is the spin-1 operator of the electron spin,  $\mathbf{I}^{(i)} = (I_x^{(i)}, I_y^{(i)}, I_z^{(i)})$  is the spin-1/2 operator of carbon nuclear spins.  $B_z$  is the external magnetic field along the NV axis.  $\gamma_e$  and  $\gamma_c$  are the gyromagnetic ratio of the electron spin and carbon nuclear spins, respectively. The hyperfine splitting  $A^{(i)} = \sqrt{(A_{\parallel}^{(i)})^2 + (A_{\perp}^{(i)})^2}$  is set to  $A^{(1)} = -1.14$  MHz and  $A^{(2)} = -0.33$  MHz as observed in the experiment.  $A_{\parallel}^{(i)}$  and  $A_{\perp}^{(i)}$  are the parallel and perpendicular hyperfine components with respect to the direction of the external magnetic field, respectively, and setting the angle between the external magnetic field and the hyperfine field as  $\theta$ , we can represent  $A_{\parallel}^{(i)} =$

$A^{(i)}\cos\theta$  and  $A_{\perp}^{(i)} = A^{(i)}\sin\theta$ .  $D_0 = 2.877$  MHz is the zero-field splitting. Next, we assume a situation without a magnetic field. With the direction of the hyperfine field as the quantization axis of carbon nuclear spins, the Hamiltonian of the electron spin and two carbon nuclear spins can be described as follows,

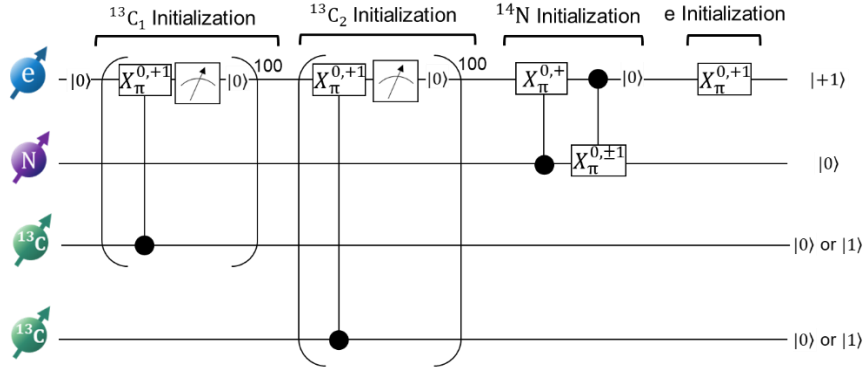
$$H = D_0 S_z^2 + \sum_{i=1}^2 \left( A^{(i)} S_z I_z^{(i)} \right), \quad (2)$$

where  $A^{(i)}$  is set to  $A^{(1)} = -1.14$  MHz and  $A^{(2)} = -0.33$  MHz as in the case with magnetic field. In calculations, the hyperfine coupling between the electron spin and the nitrogen nuclear spin is not considered because the presence or absence of a magnetic field does not affect the fidelity of the holonomic C-Z gate. Moreover, ambient effects such as environmental noise and  $T_2/T_2^*$  are not considered because we only focus on the effect of the external magnetic field on carbon nuclear spins. The results when the angle  $\theta$  between the external magnetic field and the hyperfine field is 0, 45, and 90 degrees are shown in Supplementary Fig. 1. Here, for simplicity, we consider the situation where the directions of the hyperfine fields of  $C_1$  and  $C_2$  are equal. When the direction of the external magnetic field corresponds to the direction of the hyperfine field (Supplementary Fig. 1a), only the  $I_z^{(i)}$  component is present, and the fidelity is slightly higher than that without the magnetic field. On the other hand, when the direction of the external magnetic field does not correspond to the direction of the hyperfine field (Fig. 1b, c), two orthogonal components of  $I_x^{(i)}$  and  $I_z^{(i)}$  are mixed in the Hamiltonian, and the fidelity decreases rapidly compared to the case without the magnetic field. At a magnetic field of 1000 Gauss, the fidelity is only about 98% when the angle between the external magnetic field and the hyperfine field is 45 degrees (Fig. 1b), and about 94% when the angle is 90 degrees (Fig. 1c). To obtain 99.9% fidelity, a magnetic field of more than 10000 Gauss (1T) must be applied to the carbon where the angle between the external magnetic field and the hyperfine field is less than 45 degrees.



**Supplementary Fig. 1 | Carbon spin manipulation with and without magnetic field.** a-c, Simulated Rabi frequency dependence of the fidelity of the holonomic C-Z gate based on the geometric phase between two carbon nuclear spins ( $^{13}\text{C}_1, 1.14\text{MHz}$ ;  $^{13}\text{C}_2, 0.33\text{MHz}$ ) under a zero magnetic field (blue line), 100 Gauss (green line), 1000 Gauss (red line), and 10000 Gauss (orange line). The angles between the external and hyperfine magnetic fields are set at 0 degrees (a), 45 degrees (b) and 90 degrees (c) for both carbon nuclear spins.

**Supplementary Note 2: Initialization of three nuclear spins.** The initialization of nitrogen and carbon nuclear spins is performed as shown in Supplementary Fig. 2. First, the electron spin is set to  $|0\rangle_S$  by the green laser, and then the carbon nuclear spins are initialized sequentially by projective measurement. Next, the nitrogen nuclear spin is finally initialized to  $|0\rangle_N$  by transitioning the electron spin from the  $|0\rangle_S$  to the  $|\pm 1\rangle_S$  space with a microwave  $\pi$ -pulse only for the nitrogen nuclear spin  $|\pm 1\rangle_N$ , and then by applying a radio wave  $\pi$ -pulse that resonates between  $|0\rangle_N$  and  $|\pm 1\rangle_N$  only in the electron spin  $|\pm 1\rangle_S$  space. Finally, the electron spin is initialized to  $|+1\rangle_S$  using a microwave with right-circular polarization.



**Supplementary Fig. 2 | Initialization of three nuclear spins.** The carbon nuclear spins are initialized sequentially by projective measurement, and then the nitrogen nuclear spin is initialized deterministically. Finally, the electron spin is initialized to  $|+1\rangle_S$  using a microwave with right-circular polarization.  $X_\pi^{0,+1}$  represents a  $\pi$  rotation around the X axis in the Bloch sphere spanned by  $|0\rangle$  and  $|+1\rangle$ .

**Supplementary Note 3: Single-shot measurement.** Single-shot measurement is a technique for initializing and measuring with high fidelity<sup>1-5</sup>. Nuclear spins are difficult to read directly because of their weak interaction with light. On the other hand, electron spins are read out by selectively exciting them using a red laser resonating with  $|E_y\rangle$  and observing photons emitted by relaxation. The state of the nuclear spin is swapped to the electron spin by a controlled-NOT ( $C_n\text{NOT}_S$ ) gate with a microwave, and the nuclear spin is indirectly measured by reading out the electron spin  $|0\rangle_S$  with a red laser. However, since a single measurement cannot obtain enough photons due to the experimental setup, we repeat the measurements 30 times for the nitrogen nuclear spin and 100 times for carbon nuclear spins until we get enough photons to distinguish the state. The experimental quantum circuit is shown in Supplementary Fig. 3a. The purpose of this experiment is to determine the optimal threshold for performing a single-shot measurement and to calculate the fidelity of the single-shot measurement. First, the electron spin is initialized to  $|0\rangle_S$  with a 515 nm green laser. Then, the nitrogen nuclear spin (carbon nuclear spin) is initialized to  $|0\rangle_N$  or  $|\pm 1\rangle_N$  ( $|0\rangle_C$  or  $|1\rangle_C$ ) by projective measurement. Finally, the photon number distribution of the single-shot measurement for each initial state is measured (Supplementary Fig. 3b). From the measured photon number distribution,

the optimal threshold for distinguishing between  $|0\rangle_N$  and  $|\pm 1\rangle_N$  of the nitrogen nuclear spin is 4 photons and the fidelity at the threshold is 90.5% (Supplementary Fig. 3c). The optimal thresholds for distinguishing between  $|0\rangle_C$  and  $|1\rangle_C$  of the carbon nuclear spins  $C_1$  (1.14 MHz) and  $C_2$  (0.33 MHz) are 8 and 7 photons, respectively. The fidelities with those thresholds are respectively 99.8% for  $C_1$  and 99.5% for  $C_2$  (Supplementary Fig. 3d, e). Taking carbon nuclear spins as an example, the fidelity  $F$  is calculated as

$$F = \frac{1}{2}(P_0 + P_1), \quad (3)$$

where  $P_0$  is the probability of correctly identifying  $|0\rangle_C$  and  $P_1$  is the probability of correctly identifying  $|1\rangle_C$  when a certain threshold:

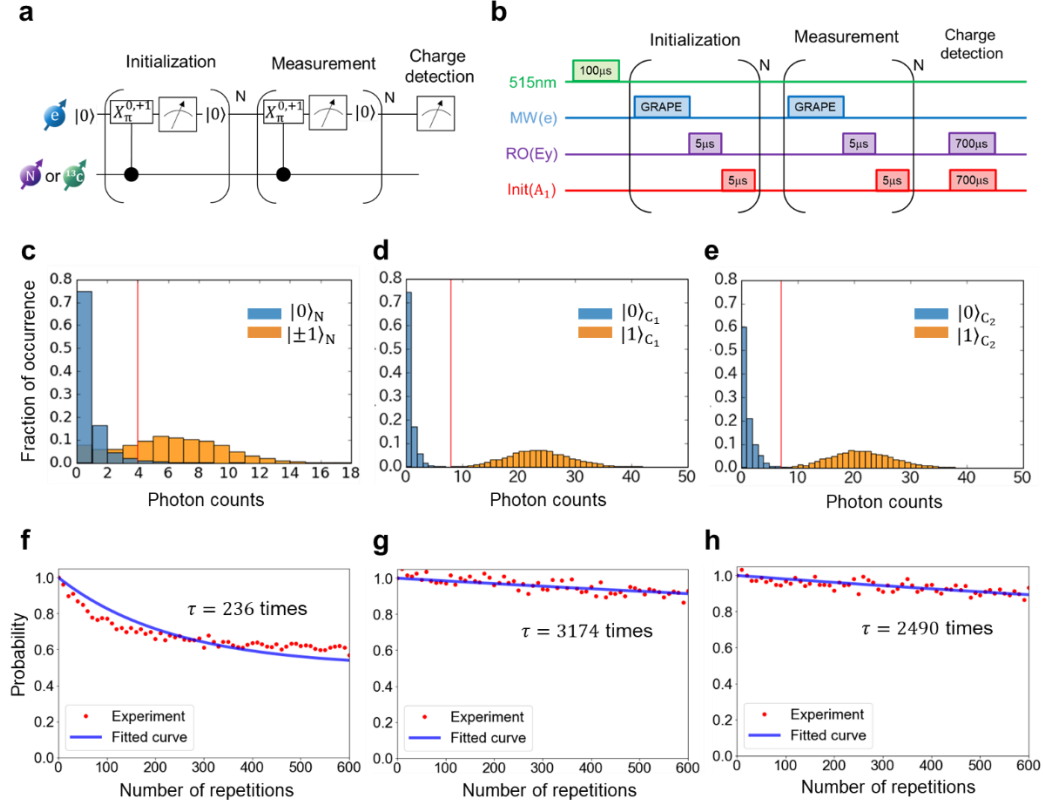
$$P_0 = \frac{P_{00}}{P_{00} + P_{01}} \quad (4)$$

$$P_1 = \frac{P_{11}}{P_{11} + P_{10}} \quad (5)$$

$P_{ij}$  ( $i, j = 0$  or  $1$ ) represents the probability that the initial state is  $|i\rangle_C$  and the measured result is  $|j\rangle_C$ . The charge state of the NV is measured at the end of the single-shot measurement, and only the  $NV^-$  events are extracted by post-selection. Although not described in the main text, charge states are measured in all experiments in the paper, and only the  $NV^-$  events are extracted.

**Supplementary Note 4: Decay by repeated measurements.** We measure the decay of the nuclear spin state for N, the number of repetitions of a series of operations ( $C_nNOT_S$  gate, measuring the electron spin and initializing the electron spin) of a single-shot measurement (Supplementary Fig. 3f-h). The fitting of the blue solid lines was obtained on  $\frac{1}{2} \exp\left(-\frac{\tau}{N}\right) + \frac{1}{2}$  for all three of Supplementary Fig. 3f-h, where  $\tau$  denotes the number of repetitions when the decay probability of the nuclear spin is  $1/e$ . These results confirm that the carbon nuclear spin is resistant to optical readout and is almost nondemolished after 100 repeated measurements. In contrast, about 8% of the nitrogen nuclear spin is demolished after 30 repeated measurements. That is the main reason for the poor results of the

single-shot measurement of nitrogen nuclear spin. If a solid immersion lens (SIL)<sup>6</sup> is implemented to increase the luminous efficiency, the number of measurements can be reduced and the fidelity can be improved.



**Supplementary Fig. 3 | Single-shot measurements of nuclear spins.** **a**, Quantum circuit to evaluate the fidelity of the single-shot measurement. The nuclear spins are initialized by projective measurement, and the photon number distribution for each initial state is obtained. Finally, the charge state of the NV is measured and only the  $\text{NV}^-$  events are extracted by post-selection.  $X_{\pi}^{0,+1}$  represents a  $\pi$  rotation around the X axis in the Bloch sphere spanned by  $|0\rangle$  and  $|+1\rangle$ . **b**, Experimental sequence. **c-e**, Fidelity evaluation of single-shot measurements. In order from c, the nitrogen nuclear spin ( $^{14}\text{N}$ ), the carbon nuclear spin ( $C_1$ ), and the carbon nuclear spin ( $C_2$ ). The fidelity is 90.5% (4 photons) for  $^{14}\text{N}$ , 99.8% (8 photons) for  $C_1$ , and 99.5% (7 photons) for  $C_2$ . The number of photons in parentheses is the threshold when the fidelity is maximized. **f-h**, Decay of the nuclear spin state against the number of repetitions  $N$  of the single-shot measurement. In order from f, the nitrogen nuclear spin ( $^{14}\text{N}$ ), the carbon nuclear spin ( $C_1$ ), and the carbon nuclear spin ( $C_2$ ). The red dotted line shows the experimental results and the blue solid line shows the fitting by the exponential function. The number of iterations  $\tau$  for which the probability is  $1/e$  from fitting is  $^{14}\text{N}$ : 236,  $C_1$ : 3174, and  $C_2$ : 2490.

**Supplementary Note 5: single qubit quantum tomography.** Quantum state tomography is one of the methods to estimate the generated quantum state. In Fig. 3c and Fig. 3d of the main text, quantum state tomography is used to estimate the nitrogen state after quantum error correction. We here explain how to obtain the Bloch vector by quantum state tomography. First, the quantum state can be expressed in the form of a density matrix as

$$\rho = \frac{I + \mathbf{r} \cdot \boldsymbol{\sigma}}{2}, \quad (6)$$

where  $I$  is the identity operator,  $\mathbf{r} = (x, y, z)$  is the Bloch vector, and  $\boldsymbol{\sigma} = (\sigma_x, \sigma_y, \sigma_z)$  is the Pauli vector. The quantum state is projected on  $\pm X$ ,  $\pm Y$ , and  $\pm Z$  axes to give components as

$$\begin{aligned} x &= \text{Tr}[\sigma_x \rho] = \langle +x | \rho | +x \rangle - \langle -x | \rho | -x \rangle, \\ y &= \text{Tr}[\sigma_y \rho] = \langle +y | \rho | +y \rangle - \langle -y | \rho | -y \rangle, \\ z &= \text{Tr}[\sigma_z \rho] = \langle +z | \rho | +z \rangle - \langle -z | \rho | -z \rangle, \end{aligned} \quad (7)$$

where  $|\pm i\rangle$  ( $i = x, y, z$ ) are the eigenstates of the Pauli operator  $\sigma_i$ . The Bloch vector  $\mathbf{r}$  is then estimated by the projected components to reconstruct the density matrix of the generated quantum state.

**Supplementary Note 6: Entanglement generation of two carbon nuclear spins.** As a preliminary step to the entanglement generation between three nuclear spins described in the main text, we first generated the entanglement between two carbon nuclear spins, which requires the C-Z gate between them. This is solved by applying the holonomic C-Z gate based on the geometric phase with the help of the electron spin, similar to the three-qubit entanglement generation described in the main text. In this case, we added a  $\pi$ -phase only for  $|1\ 1\rangle_{C_1, C_2}$  ( $|1\ 1\rangle_{C_1, C_2} \rightarrow -|1\ 1\rangle_{C_1, C_2}$ ). The quantum circuit of the experiment is shown in Supplementary Fig. 4a. First, the two carbon nuclear spins are initialized to  $|0\ 0\rangle_{C_1, C_2}$ ,  $|0\ 1\rangle_{C_1, C_2}$ ,  $|1\ 0\rangle_{C_1, C_2}$ , or  $|1\ 1\rangle_{C_1, C_2}$  by projective measurement, and the electron spin is also initialized into  $|+1\rangle_S$  using microwaves. Entanglement was then generated between the two

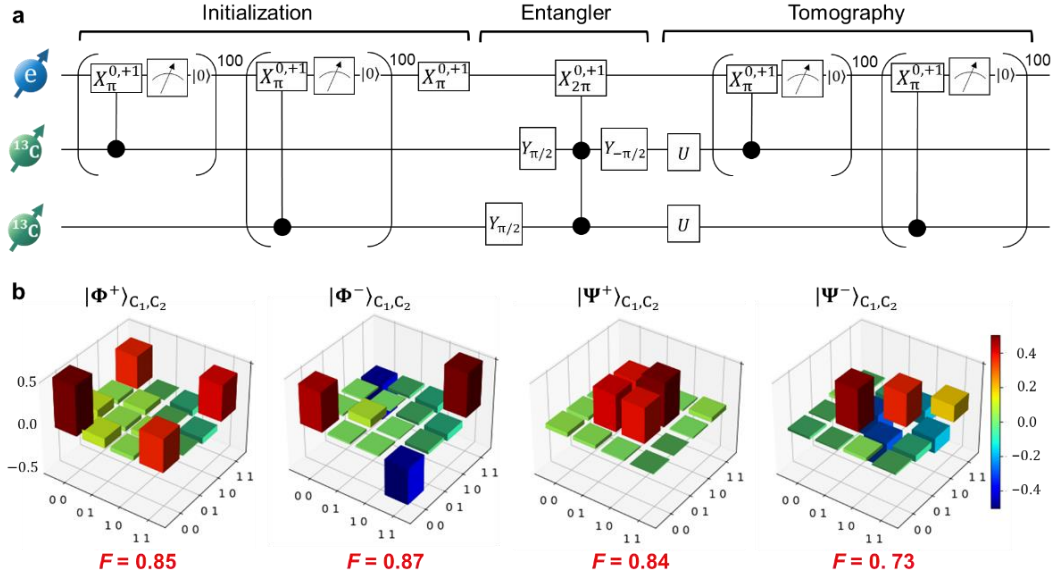
carbon nuclear spins by the Hadamard gates with a radio wave and the C-Z gate with a microwave, and then the states are estimated by the quantum state tomography, where individual carbon nuclear spin is projected on the X, Y, or Z basis based on a single-shot measurement (Supplementary Table. 1). We apply the quantum state tomography on the four generated entangled states corresponding to  $|\Phi^+\rangle_{C_1,C_2}, |\Phi^-\rangle_{C_1,C_2}, |\Psi^+\rangle_{C_1,C_2}, |\Psi^-\rangle_{C_1,C_2}$  and estimate their fidelities, which are respectively 85%, 87%, 84%, and 73% (Supplementary Fig. 4b). Fidelity is calculated using the following procedure. First, the density matrix  $\rho$  of the entangled states is represented by<sup>7</sup>

$$\rho = \frac{1}{2^2} \sum_{i,j=0}^3 r_i r_j \sigma_i \sigma_j, \quad (8)$$

where  $r_i$  and  $r_j$  are real numbers and  $r_0 = 1$ .  $\sigma_0 = I$  is the identity operator for a single qubit, and  $\sigma_1 = \sigma_x$ ,  $\sigma_2 = \sigma_y$ , and  $\sigma_3 = \sigma_z$  are Pauli operators. Also,  $r_i r_j$  are the expectation values of the operators  $\langle \sigma_i \sigma_j \rangle = \text{Tr}[\sigma_i \sigma_j \rho]$ , which can be obtained from the experiment. The fidelity  $F$  to the ideal state  $|\psi_{\text{id}}\rangle$  is

$$F = \text{Tr}[|\psi_{\text{id}}\rangle\langle\psi_{\text{id}}|\rho]. \quad (9)$$





**Supplementary Fig. 4 | Entanglement generation of two carbon nuclear spins.** **a**, Quantum circuit of entanglement generation between two carbon nuclear spins. For the two-qubit operation between carbon nuclear spins, the holonomic C-Z gate based on the geometric phase is applied as in the three-qubit operation.  $X_{\pi}^{0,+1}$  represents a  $\pi$  rotation around the X axis in the Bloch sphere spanned by  $|0\rangle$  and  $|+1\rangle$ . **b**, The real part of the density matrix of Bell states reconstructed by two-qubit state tomography.

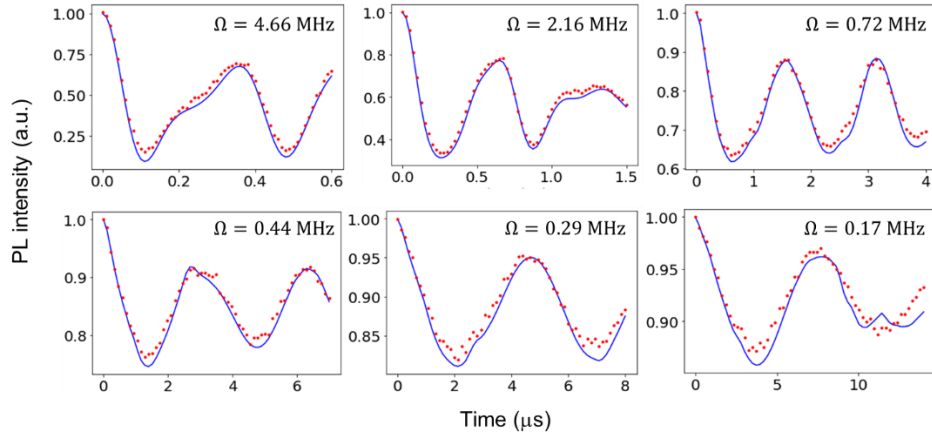
**Supplementary Table. 1 | Basis transformations for tomography measurements.** When we measure in the X or Y basis, basis transformations are performed with a  $\pi/2$  pulse of radio waves before single-shot measurements.  $Y_{\pi/2}$  represents a  $\pi/2$  rotation around the Y axis.

Projection	$\langle\sigma_x\rangle$	$\langle\sigma_y\rangle$	$\langle\sigma_z\rangle$
$U$	$Y_{\pi/2}$	$X_{\pi/2}$	$I$

**Supplementary Note 7: Rabi oscillation of the electron spin.** The measured Rabi oscillation of the electron spin are shown as red dots in Supplementary Fig. 5. The blue lines are simulated with the system Hamiltonian as follows,

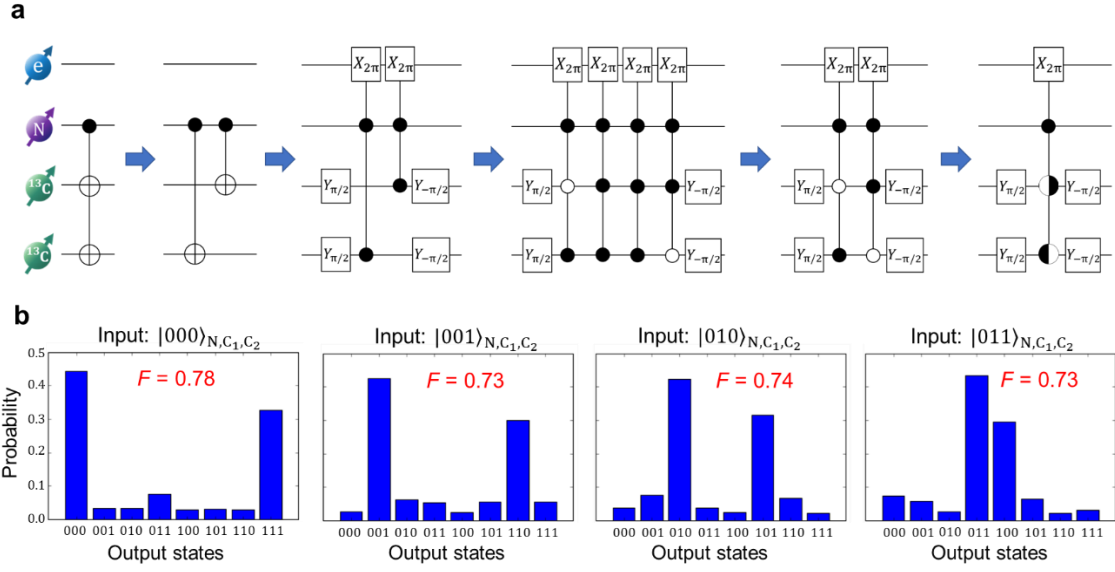
$$H = D_0 S_z^2 + A^N S_z I_z^N + \sum_{i=1}^4 \left( A^{(i)} S_z I_z^{(i)} \right), \quad (10)$$

where  $A^N = -2.168$  MHz is the hyperfine coupling between the electron spin and the nitrogen nuclear spin,  $\mathbf{I}^N = (I_x^N, I_y^N, I_z^N)$  is the spin-1 operator of the nitrogen nuclear spin,  $\mathbf{I}^{(i)} = (I_x^{(i)}, I_y^{(i)}, I_z^{(i)})$  is the spin-1/2 operator of carbon nuclear spins.  $A^{(i)}$  are set to  $A^{(1)} = -1.14$  MHz,  $A^{(2)} = -0.33$  MHz,  $A^{(3)} = -0.10$  MHz and  $A^{(4)} = -0.10$  MHz. Although  $A^{(3)}$  and  $A^{(4)}$  cannot be estimated from the splitting in the ODMR spectrum, they can be roughly estimated from best fitting to the measured Rabi oscillation. We then estimated the hyperfine coupling of the third carbon is around  $A^{(3)} = -0.10$  MHz, and shown as "Estimated Value" with some uncertainty in Fig. 4 of the main text. The measured ODMR spectrum shown in Fig. 1d of the main text is also fitted with the Hamiltonian shown in Eq. (10).

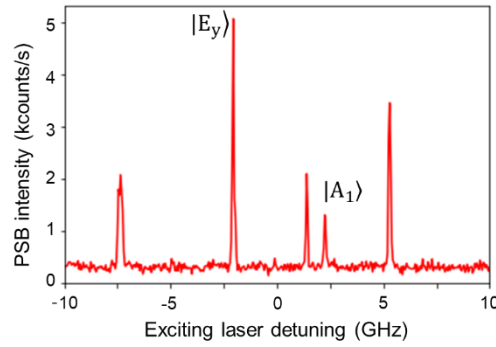


**Supplementary Fig. 5 | Rabi oscillation of the electron spin.** Measured (red dots) and simulated (blue lines)

Rabi oscillation as a function of Rabi frequency  $\Omega$  dependent on the amplitude of the applied microwaves.



**Supplementary Fig. 6 | Entanglement generation of three nuclear spins.** **a**, Equivalent circuit of the encoding of Fig. 2a in the main text. The Hadamard gate is constructed with a  $\pi/2$  pulse of radio waves, and a holonomic C-Z gate based on the geometric phase is used to add a  $\pi$  phase to  $|101\rangle_{N,C_1,C_2}$  and  $|110\rangle_{N,C_1,C_2}$ . **b**, Experimental results of entanglement generation for different initial carbon nuclear spin states in Fig. 2a and b in the main text. SPAM errors are included and the fidelities of both are low, but the classical correlation is confirmed.



**Supplementary Fig. 7 | PLE spectrum.** The  $|A_1\rangle$  state is used for electron spin initialization and the  $|E_y\rangle$  state is used for electron spin measurement.

## Supplementary References

1. Drau, A., Spinicelli, P., Maze, J. R., Roch, J.-F., and Jacques, V. Single-shot readout of

multiple nuclear spin qubits in diamond under ambient conditions. *Physical Review Letters* **110** (2013).

2. Liu, G.-Q. *et al.* Single-shot readout of a nuclear spin weakly coupled to a nitrogen-vacancy center at room temperature. *Phys. Rev. Lett.* **118**, 150504 (2017).
3. Neumann, P. *et al.* Single-shot readout of a single nuclear spin. *Science* **329**, 542–544 (2010).
4. Robledo, L. *et al.* High-fidelity projective read-out of a solid-state spin quantum register. *Nature* **477**, 574–578 (2011).
5. Waldherr, G. *et al.* Quantum error correction in a solid-state hybrid spin register. *Nature* **506**, 204–207 (2014).
6. Marseglia, L. *et al.* Nanofabricated solid immersion lenses registered to single emitters in diamond. *Applied Physics Letters* **98**, 133107–133107–3 (2011).
7. James, D., Kwiat, P., Munro, W. & White, A. Measurement of qubits. *Phys. Rev. A* **64**, 052312 (2001).